atmosphere

MDPI

Article

Influence of North Atlantic Sea Surface Temperature Anomalies on Tibetan Plateau Vortex Frequency Variability

Likang Xu [1,2], Panjie Qiao [1,2,*], Zaibo Zhao [1,2], Tingting Xue [1,2] and Xu Li [1,2]

[1] Faculty of Science, Kunming University of Science and Technology, Kunming 650500, China; 13103276032@163.com (L.X.); zaibo.zhao@stu.kust.edu.cn (Z.Z.); tingtingxue@kust.edu.cn (T.X.); lixucn@kust.edu.cn (X.L.)
[2] Yunnan Key Laboratory of Complex Systems and Brain-Inspired Intelligence, Kunming 650500, China
* Correspondence: qiaopj@kust.edu.cn

Abstract

This study investigates the frequency of Tibetan Plateau vortices (TPVs) and their statistical relationship with global sea surface temperature (SST) anomalies. The results show that TPV frequency exhibits pronounced seasonal and interannual variability. Annual TPV frequency generally ranges from 50 to 70 events, with short-lived TPVs, particularly those lasting two days, accounting for the majority of occurrences. TPV activity is most active during summer and relatively weak during autumn and winter. Lagged correlation analyses reveal that the North Atlantic exhibits the strongest statistical linkage with TPV frequency among all global ocean basins. After removing the linear trends, the maximum correlation occurs when North Atlantic SST anomalies lead TPV frequency anomalies by approximately two months, indicating a robust lagged relationship between the two variables. Further circulation analyses suggest that North Atlantic SST anomalies are closely associated with large-scale atmospheric circulation anomalies over the North Atlantic–Eurasian sector prior to TPV-active months. Anomalous geopotential height and wind fields at 500 hPa, together with upper-level wind anomalies at 200 hPa, indicate significant adjustments of the Eurasian midlatitude circulation and upper-level westerly jet associated with North Atlantic SST variability. During TPV-active months, enhanced upper-level divergence, strengthened upward motion, and intensified cyclonic anomalies emerge over the Tibetan Plateau, providing favorable dynamical conditions for TPV formation and development. Overall, the results reveal a statistically robust linkage between North Atlantic SST anomalies and TPV frequency variability and provide new insight into the associated large-scale circulation background over the Tibetan Plateau.

Keywords: Tibetan Plateau vortex; North Atlantic; global sea surface temperature; lagged correlation

Check for updates

Academic Editor: Anthony R. Lupo

Received: 22 April 2026
Revised: 28 May 2026
Accepted: 9 June 2026
Published: 10 June 2026

1. Introduction

The Tibetan Plateau (TP), located in the interior of Asia, is characterized by its exceptionally high altitude and complex topography, which enable it to play an important role in the global climate system [1–4]. Its complex topography and unique atmospheric circulation support the development of distinctive weather systems over the TP, among which the Tibetan Plateau vortex (TPV) is one of the most important [5–11]. As a frequently occurring mesoscale cyclonic system, the TPV exerts significant influences on weather and climate over the plateau and its surrounding regions.

Atmosphere **2026**, *17*, 595

https://doi.org/10.3390/atmos17060595

TPVs are primarily generated over the central and western TP [12,13]. They are mesoscale weather systems typically centered in the mid-troposphere, with a shallow vertical structure and a relatively short lifetime of about 1–3 days. TPV activity is strongly seasonal, with peak occurrence during the warm season, especially in summer [14–18]. TPVs are closely associated with heavy precipitation over the TP and are among the most important weather systems responsible for local rainstorms, persistent rainfall, and related secondary disasters. Under favorable large-scale circulation conditions, TPVs can propagate eastward along shear lines, convergence zones, or background flows [19] and may further intensify over Southwest China, the Jianghan Plain, and the Yangtze River basin, thereby contributing to heavy rainfall in these regions [20–25]. For example, during the catastrophic 1998 flood over the Yangtze River basin, eight low-pressure systems originating from the TP contributed to eight major flood peaks in the middle and lower reaches of the Yangtze River [14].

Previous studies have primarily focused on individual TPV cases, their formation and development mechanisms, and their downstream impacts, providing substantial insight into their thermodynamic background and interactions with large-scale circulation [26–28]. In contrast, studies examining TPV activity from a climatic perspective, particularly those addressing its frequency and spatiotemporal variability, remain limited. Moreover, the potential influence of oceanic thermal anomalies on TPV activity through large-scale circulation anomalies has not been systematically investigated.

Sea surface temperature (SST) anomalies are an important manifestation of air–sea interaction and play a crucial role in modulating large-scale atmospheric circulation and climate variability. SST anomalies, particularly those over the North Atlantic, can influence atmospheric circulation over remote regions by exciting Rossby wave trains that propagate across the mid–high latitudes [29–32]. In the TP region, air–sea interaction and SST anomalies have also been shown to modulate atmospheric circulation and potential vorticity activity over and around the TP [33–36]. For example, Ma et al. linked anomalously warm SST in the Indian Ocean to enhanced potential vorticity activity over the TP and severe flooding along the Yangtze River during the summer of 2020 [37]. Sheng et al. further demonstrated that the North Atlantic tripole SST mode can significantly influence surface potential vorticity over the TP during the boreal summer [36]. However, how SST anomalies affect interannual variations in TPV frequency and the underlying physical mechanisms remain unclear.

On this basis, this study first investigates the spatiotemporal characteristics of TPV activity, then identifies key oceanic regions where SST anomalies are closely linked to interannual variations in TPV frequency, and finally examines the associated atmospheric circulation mechanisms.

2. Materials and Methods

2.1. Data

The TPV dataset used in this study was obtained from the National Tibetan Plateau Data Center and spans the period from 1951 to 2021. The dataset was developed by Lin Zhiqiang's research team based on multiple reanalysis products using an objective identification and tracking algorithm specifically designed for TPVs [38]. The dataset provides a long-term record of TPV activities, including information on vortex location, radius, intensity, lifetime, occurrence frequency, and movement tracks (http://www.sciencedb.cn/dataSet/handle/556, accessed on 14 October 2024). In addition, the dataset includes monthly TPV frequency statistics derived from the original daily records. In the present study, we primarily focus on monthly TPV frequency. Given the relatively short lifetime and synoptic-scale characteristics of individual TPVs, monthly

TPV frequency was used to examine interannual variability as well as its relationship with large-scale climate anomalies. Atmospheric and oceanic variables used in this study, including SST, geopotential height, horizontal wind, pressure vertical velocity, divergence, and relative vorticity, were obtained from the European Centre for Medium-Range Weather Forecasts' ERA5 reanalysis. All variables have a horizontal resolution of 0.25° × 0.25°. Here, divergence refers to the horizontal divergence of velocity, which represents the rate at which air is spreading out horizontally from a point per square meter. Positive divergence values indicate horizontal air outflow (divergence), while negative values indicate horizontal air convergence (convergence). Relative vorticity represents the local rotation of air in the horizontal plane about a vertical axis, relative to a fixed point on the surface of the Earth.

2.2. Methods

For each SST grid point, the time series was first standardized by removing the climatological monthly mean and dividing by the corresponding monthly standard deviation. The standardized anomaly was calculated as

$$X_i(t) = \frac{\widetilde{X}_i(t) - mean(\widetilde{X}_i(t))}{std(\widetilde{X}_i(t))} \tag{1}$$

where *mean* and *std* represent the climatological monthly mean and standard deviation of the corresponding time series, respectively. The TPV frequency series was standardized using the same procedure.

Prior to the analysis, both the SST anomaly series at each grid point and the TPV frequency anomaly series were linearly detrended to reduce the influence of long-term climate trends and low-frequency variability. Pearson lag correlations between TPV frequency and SST anomalies were calculated for each global ocean grid point. The processed SST anomaly time series $X_i(t)$ was correlated with the TPV frequency anomaly series $Y(t+\tau)$, where τ denotes the lag time. The cross-correlation function is written as

$$R_i(\tau) = \frac{Cov(X_i(t), Y(t+\tau))}{\sigma_{X_i}\sigma_Y} \tag{2}$$

where $Cov(\cdot)$ denotes covariance, and σ_{X_i} and σ_Y represent the standard deviations of the SST anomaly time series at grid point i and the TPV frequency anomaly time series, respectively. The lag time τ ranged from 0 to 11 months. A positive τ indicates that SST anomalies lead TPV frequency. For example, $\tau = 2$ represents the correlation between SST anomalies and TPV frequency anomalies two months later.

For each SST grid point i, the maximum correlation coefficient with TPV frequency is defined as $R_i^{max} = max|R_i(\tau)|$. To evaluate the statistical significance of the lagged correlations, the order of years in the TPV frequency anomaly series was randomly shuffled 1000 times while preserving the intra-annual variability within each year. The SST anomaly series was kept unchanged. Lagged cross-correlations were recalculated for each shuffled realization to obtain a null distribution of correlation coefficients associated with random variability. The 99th percentile of the absolute values of the shuffled correlations was used as the significance threshold. Grid points with correlation coefficients exceeding this threshold were regarded as statistically significant at the 99% confidence level.

3. Results

3.1. Statistical Characteristics of TPVs

We first examine the frequency, duration, and seasonal characteristics of TPVs during 1951–2021 (Figure 1). The probability density distribution of annual TPV frequency shows that most years experience approximately 50–70 TPV events, with only a few years exhibiting exceptionally high or low frequencies (Figure 1a). TPVs are predominantly short-lived systems, with two-day events being the most common, while events lasting longer than five days are relatively rare and only a few persist for more than ten days (Figure 1b). TPV frequency exhibits pronounced seasonal variability (Figure 1c). TPV activity reaches its maximum in summer, accounting for the largest proportion of the annual total, followed by spring. In contrast, TPV frequency decreases markedly in autumn and reaches its minimum in winter.

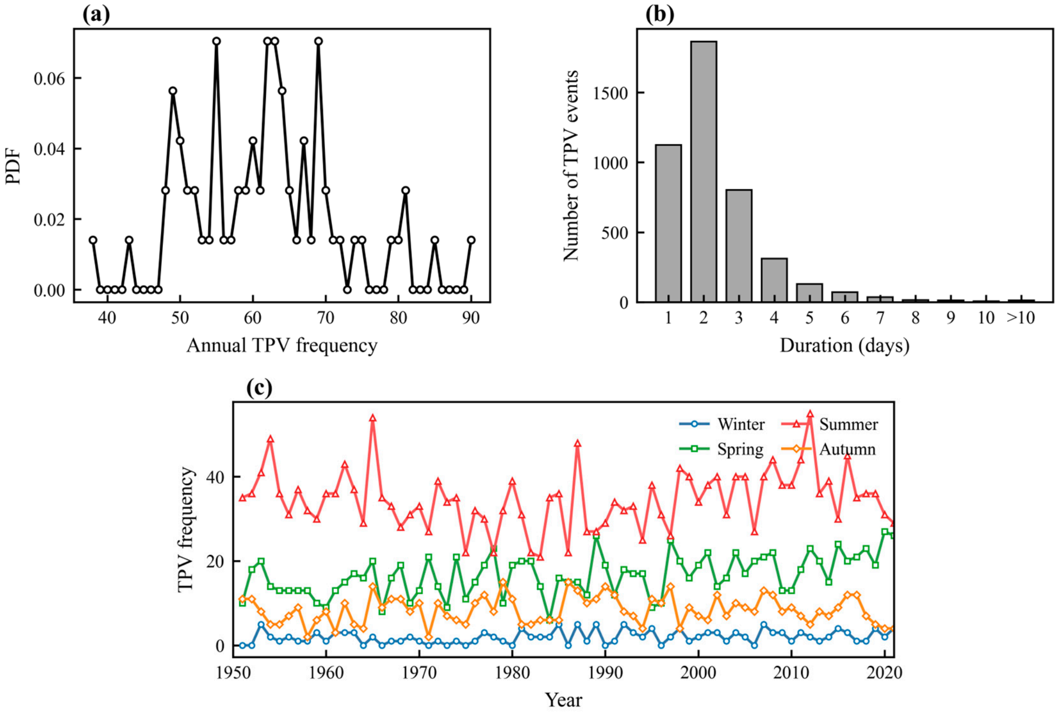

Figure 1. Statistical characteristics of Tibetan Plateau vortices (TPVs) during 1951–2021: (**a**) probability density function (PDF) of annual TPV frequency; (**b**) TPV duration distribution; (**c**) seasonal variation in TPV frequency.

3.2. Relationship Between Global SST and TPVs

To examine the potential antecedent influence of sea surface temperature anomalies (SSTAs) on the frequency of TPVs, correlation coefficients were calculated between global SSTAs leading by 0–11 months and TPV frequency. Figure 2 shows the spatial distribution of these correlations for different lead times. Here, the lead month denotes the time by which SSTAs precede variations in TPV frequency; a larger lead indicates that the SSTAs occurred earlier. By comparing the spatial patterns and statistical significance of the correlations at different lead times, key oceanic regions significantly associated with TPV frequency can be identified, together with the lead times at which these relationships are strongest.

As shown in Figure 2, statistically significant correlations are not uniformly distributed across the global oceans but are concentrated in several distinct regions, indicating substantial geographical differences in the strength of the SSTA–TPV relationship. Among these regions, the North Atlantic exhibits the most prominent and persistent signal. Significant correlation centers recur in nearly the same area across multiple lead months, and the corresponding spatial patterns remain coherent over time. Notably, the strongest correlations between North Atlantic SSTAs and TPV frequency occur at a lead time of approximately two months, suggesting a pronounced delayed relationship between the two variables. In contrast, although localized significant correlations are also detected over other ocean basins, including the Pacific and Indian Oceans, these signals are generally weaker, more spatially scattered, and confined to only a few isolated lead months. The pronounced contrast in both spatial coherence and temporal persistence suggests that the statistical relationship between North Atlantic SSTAs and TPV frequency is considerably more robust than that found in other oceanic regions. These results indicate that North Atlantic SSTAs are closely linked to interannual variations in TPV frequency and may provide a useful precursor signal for TPV variability.

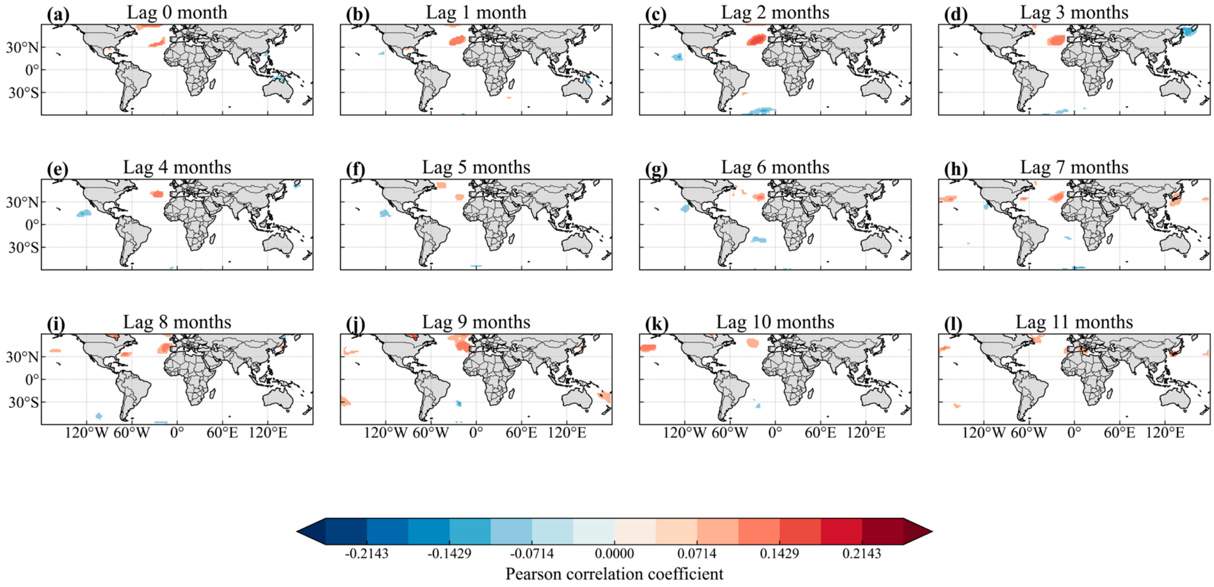

Figure 2. Spatial distribution of statistically significant Pearson lag correlations between global sea surface temperature (SST) and Tibetan Plateau vortex (TPV) frequency at different lead times. Panels (**a**–**l**) correspond to SST leading TPV frequency by 0–11 months, respectively. Only grid points passing the significance test are shown; non-significant areas are left blank.

To further summarize the lagged relationship over the key North Atlantic region, a regional North Atlantic Sea Surface Temperature Index (NASSTI) was constructed based on the spatial distribution of significant correlations shown in Figure 2. Specifically, the region bounded by 30–50° N and 300–360° E was selected as the key North Atlantic region. To account for the meridional variation in grid-cell area, cosine-latitude weighting was applied when calculating the regional mean. Standardized regression coefficients were then calculated between the preprocessed monthly NASSTI series and the monthly TPV frequency anomaly series at lead times of 0–11 months. As shown in Figure 3, the regression coefficient reaches its maximum when NASSTI leads TPV frequency by two months, with a value of 0.17, significant at the 95% confidence level.

To reduce the influence of long-term climate trends on the correlation analysis, both the SST time series at each grid point and the TPV frequency series were linearly detrended. The significant correlation between North Atlantic SSTAs and TPV frequency remained evident after detrending, with the strongest correlation occurring when SSTAs led TPV frequency by approximately two months. This result suggests that the linkage between North Atlantic SST variability and TPV activity is not solely driven by long-term trends, but primarily reflects coherent interannual variability. Based on the strongest lead–lag relationship identified above, the NASSTI was advanced by two months relative to the

TPV frequency series. The original non-detrended NASSTI and TPV frequency series were then averaged annually and standardized for comparison. As shown in Figure 4, the two standardized series exhibit broadly consistent temporal variations. The Pearson correlation coefficient between the two series is 0.54, which is statistically significant at the 95% confidence level.

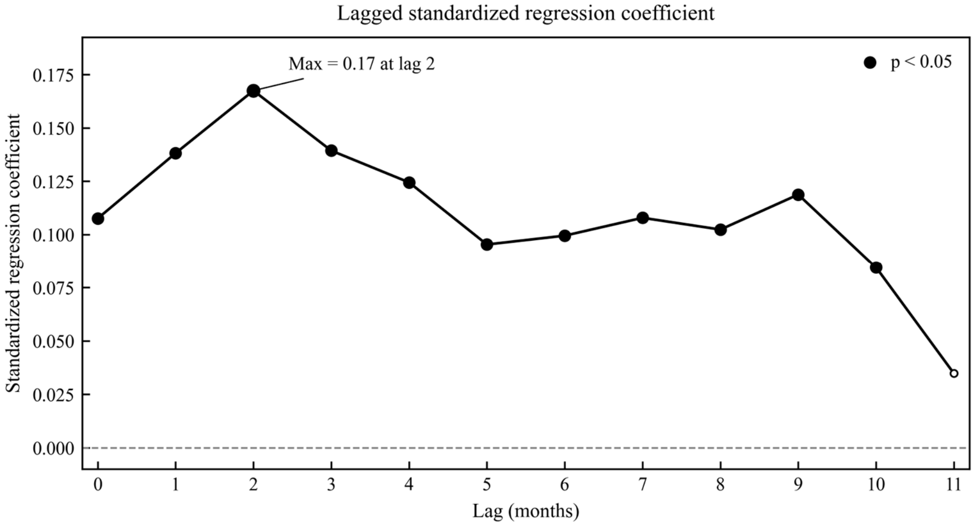

Figure 3. Standardized regression coefficients between the North Atlantic sea surface temperature index (NASSTI) leading by 0–11 months and TPV frequency. Filled dots denote coefficients significant at $p < 0.05$.

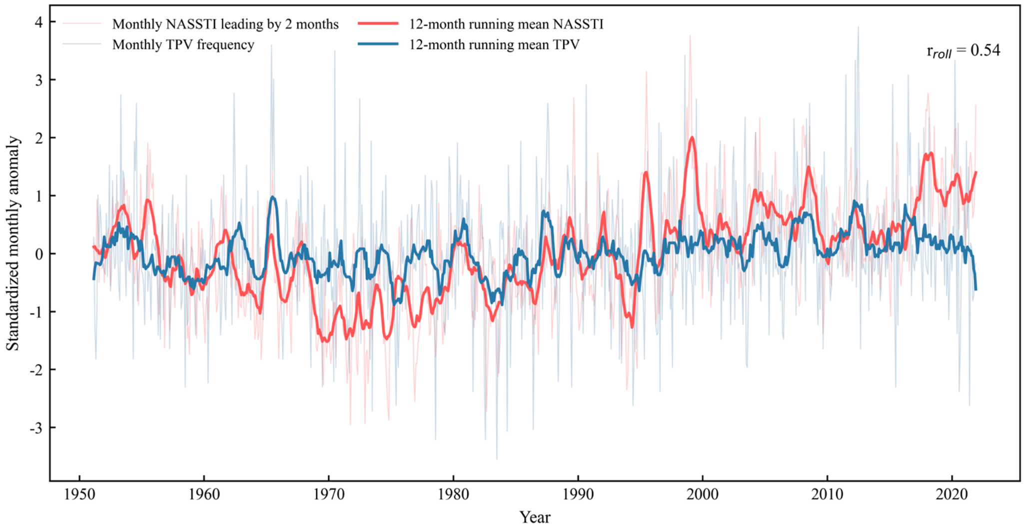

Figure 4. Time series of the standardized NASSTI (leading the TPV frequency by two months) and the standardized TPV frequency during 1951–2021. Light-colored thin lines denote the monthly standardized series, while solid thick lines represent the corresponding 12-month running means.

3.3. Mechanisms Linking North Atlantic SSTAs to TPV Variability

As the correlation between North Atlantic SSTAs and TPV frequency reaches its maximum when the SSTAs lead by approximately two months, lagged regression analyses were further performed to investigate the possible large-scale circulation background linking North Atlantic SST variability to TPV frequency. Specifically, the NASSTI leading the TPV frequency by two months, one month, and at zero lag was separately regressed onto the 500 hPa geopotential height and wind fields, and the results are shown in Figure 5. At the two-month lead (Figure 5a), the 500 hPa geopotential height regression field associated with the NASSTI already exhibits pronounced anomalies over the North Atlantic and the mid–high latitudes of Eurasia. Positive geopotential height anomalies dominate over the North Atlantic, while alternating positive and negative anomalies appear downstream across Eurasia, forming a wave-train-like spatial structure. Meanwhile, the associated wind anomalies are mainly distributed along the midlatitude westerly jet, suggesting that North Atlantic SSTAs are closely linked to large-scale circulation anomalies over the Eurasian continent.

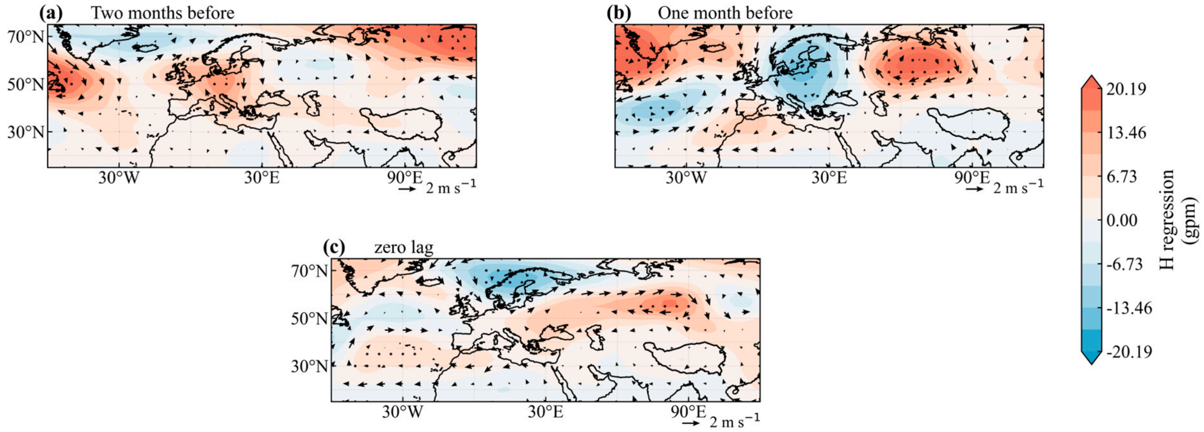

Figure 5. Regression patterns of 500 hPa geopotential height (shading; units: gpm) and horizontal wind fields (vectors; units: m s^{-1}) onto the NASSTI when the NASSTI leads the TPV frequency by (**a**) two months, (**b**) one month, and (**c**) zero mouths. The reference vector shown at the lower right corner of each panel. Black dots indicate regions passing the 90% significance test.

At the one-month lead (Figure 5b), the circulation anomalies over the mid–high latitudes of Eurasia become stronger and extend farther eastward. A pronounced negative geopotential height anomaly appears near the Ural Mountains, while positive height anomalies dominate over East Asia, forming a clear trough–ridge configuration. The associated wind anomalies are also intensified, indicating that the large-scale circulation anomalies related to the NASSTI exhibit considerable persistence and downstream development over Eurasia. At zero lag (Figure 5c), the circulation anomalies associated with the NASSTI further extend toward East Asia and the TP region. Negative geopotential height anomalies persist over the mid–high latitudes north of the TP, while positive anomalies remain over East Asia. Meanwhile, significant wind anomalies are observed around the TP. Such a trough–ridge circulation pattern may alter the position and intensity of the westerly jet near the TP and further modulate vorticity transport and large-scale dynamical conditions over the TP region, thereby influencing TPV frequency.

To further investigate the possible dynamical mechanism linking North Atlantic SSTAs to TPV frequency, regression analyses of 200 hPa zonal wind (U) and meridional wind (V) anomalies onto the standardized NASSTI were performed. Since the 200 hPa level corresponds to the core region of the midlatitude westerly jet over Eurasia, variations in the upper-level wind field can effectively reflect large-scale circulation anomalies over the Eurasian continent.

At the two-month lead (Figure 6a,d), the zonal wind regression field exhibits negative anomalies over the midlatitude North Atlantic and positive anomalies extending from northern Europe to western Siberia, indicating a significant adjustment of the upper-level westerly jet over Eurasia. Meanwhile, the meridional wind regression field displays alternating positive and negative anomaly centers over the North Atlantic–European sector, forming a wave-like anomaly structure across the Eurasian mid–high latitudes.

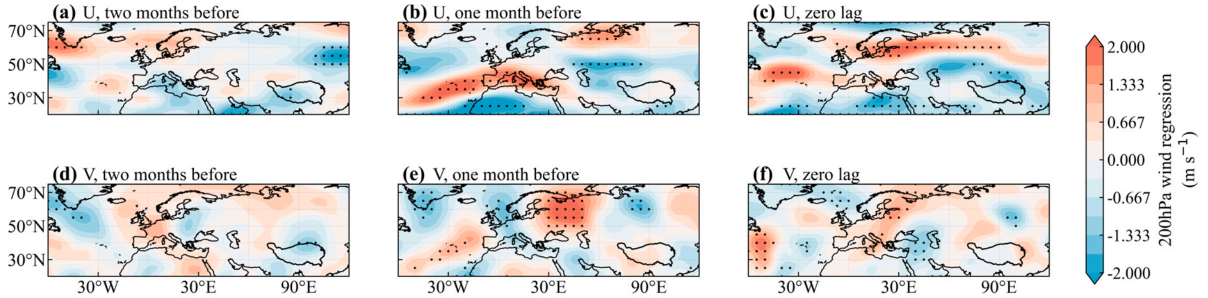

Figure 6. Regression patterns of 200 hPa wind anomalies associated with the standardized NASSTI. Panels (**a**–**c**) show regression coefficients of zonal wind (U), and panels (**d**–**f**) show regression coefficients of meridional wind (V) (shading; units: m/s). Panels (**a**,**d**), (**b**,**e**), and (**c**,**f**) correspond to the NASSTI leading TPV frequency by two months, one month, and zero lag, respectively. Black dots indicate regions statistically significant at the 90% confidence level.

At the one-month lead (Figure 6b,e), the positive zonal wind anomalies further intensify and extend eastward across northern Eurasia, while negative zonal wind anomalies persist over the midlatitude Eurasian sector south of the jet core, suggesting further adjustment of the upper-level westerly jet structure. In contrast, the meridional wind regression field mainly exhibits localized positive and negative anomaly centers over Eurasia without a clearly organized wave-train pattern.

At zero lag (Figure 6c,f), negative zonal wind anomalies appear around the TP and its surrounding regions, while positive anomalies remain over northern Eurasia, implying a weakening of the upper-level westerlies near the TP. The meridional wind regression field still exhibits noticeable anomaly centers over Eurasia, although the wave-like structure becomes relatively weaker compared to the earlier lead times.

To further examine the local circulation anomalies associated with TPV frequency over the TP, composite anomalies of 400 hPa vertical velocity, 200 hPa divergence, and 500 hPa relative vorticity were analyzed for the two months before, one month before, and the TPV-active month (Figure 7). The 200 hPa divergence, 400 hPa pressure vertical velocity, and 500 hPa relative vorticity were used to represent upper-level divergence, vertical motion, and mid-level cyclonic circulation anomalies associated with TPV activity over the TP, respectively.

During the two lead periods (Figure 7a,b,d,e,g,h), the anomalous signals over the TP are generally weak and spatially scattered, with no clearly organized large-scale structure. In contrast, during the TPV-active month (Figure 7c,f,i), pronounced circulation anomalies emerge across much of the TP and its surrounding regions. At 400 hPa, pronounced negative anomalies of vertical velocity (omega) are mainly concentrated over the central and eastern TP, indicating enhanced large-scale ascent. Simultaneously, positive divergence anomalies appear at 200 hPa, suggesting strengthened upper-level divergence and enhanced mass outflow aloft. At 500 hPa, widespread positive relative vorticity anomalies are observed over the Plateau, indicating enhanced cyclonic circulation in the midtroposphere. The simultaneous occurrence of intensified midlevel ascent, enhanced upper-level divergence, and strengthened cyclonic vorticity anomalies suggests the establishment of a dynamically favorable circulation configuration for TPV activity over the TP. Compared with the relatively weak and disorganized anomalies during the lead periods, these circulation signals become considerably stronger and more spatially coherent during the TPV-active month, indicating that the atmospheric dynamical response associated with TPV activity is most pronounced during the mature stage of TPV development. Here, the TPV-active month was defined as a month in which the standardized monthly TPV frequency anomaly exceeded the prescribed threshold.

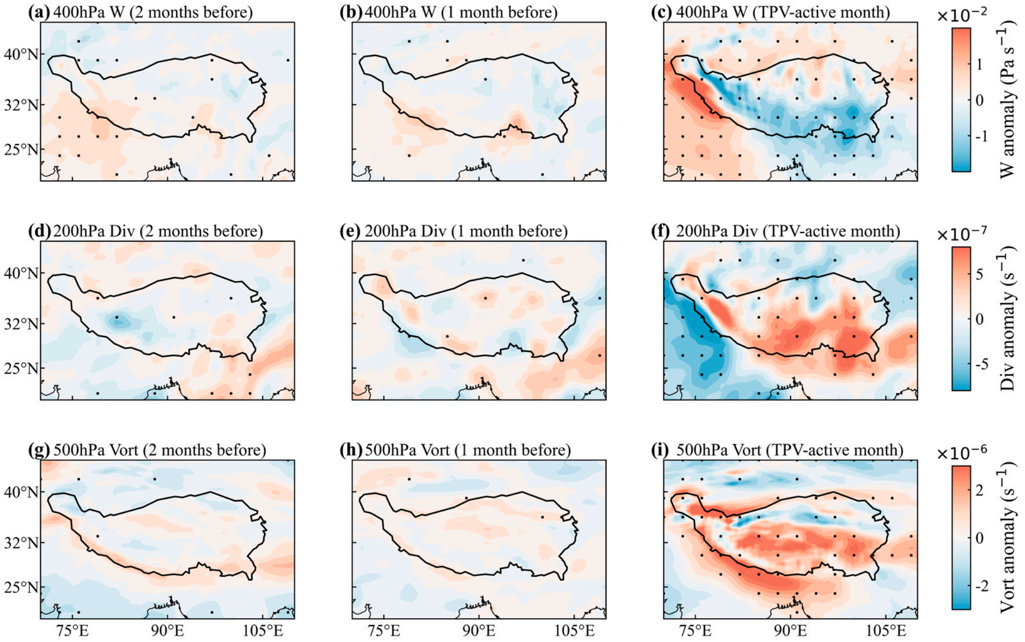

Figure 7. Anomalies of 400 hPa pressure vertical velocity (shading, units: Pa s^{-1}), 200 hPa divergence (shading, units: s^{-1}), and 500 hPa relative vorticity (shading, units: s^{-1}) during different periods. Black dots indicate regions passing the 90% significance test.

4. Conclusions

This study investigated the spatiotemporal characteristics of Tibetan Plateau vortex (TPV) frequency and its statistical relationship with global sea surface temperature (SST) anomalies. The results show that TPV frequency exhibits pronounced seasonal and interannual variability. The annual TPV frequency is mainly concentrated within 50–70 events, with short-lived TPVs dominating the total occurrences, particularly those lasting for two days. In terms of seasonal variation, TPVs occur most frequently during summer, whereas their activity is relatively weak in autumn and winter. Lagged correlation analyses between global SST anomalies and TPV frequency reveal that the North Atlantic exhibits the strongest statistical linkage with TPV activity among all ocean basins. After removing the linear trends, the maximum correlation occurs when North Atlantic SST anomalies (SSTAs) lead TPV frequency anomalies by approximately two months. This result indicates that the relationship between North Atlantic SST and TPV activity mainly reflects coherent variability on interannual timescales rather than being solely attributable to their common long-term trends.

Further circulation analyses suggest that North Atlantic SSTAs may influence TPV activity through modulation of the large-scale atmospheric circulation over the Eurasian mid–high latitudes. Prior to TPV-active months, anomalous 500 hPa geopotential height and wind fields are already established over the North Atlantic–Eurasian sector and exhibit a wave-like circulation structure. Meanwhile, anomalous wind signals at 200 hPa are mainly distributed along the Eurasian midlatitude westerly jet, indicating a close relationship between North Atlantic SSTAs and variations in the upper-level westerly circulation. As the lead time decreases, these large-scale circulation anomalies gradually extend downstream across Eurasia and further influence the atmospheric circulation background around the Tibetan Plateau (TP). During TPV-active months, pronounced local dynamical anomalies emerge over the TP and its surrounding regions, including enhanced upper-level divergence at 200 hPa, intensified upward motion at 400 hPa, and strengthened positive relative vorticity anomalies at 500 hPa. These anomalies correspond to enhanced upper-level mass divergence, stronger midtropospheric ascent, and intensified cyclonic circulation, respectively, together forming a dynamically favorable environment for TPV generation and maintenance. Compared with the relatively weak and spatially scattered anomalies during the lead periods, the circulation anomalies during TPV-active months become much stronger and more spatially coherent, suggesting that TPV development is closely associated with the synergistic effects of multilevel dynamical processes over the TP.

5. Discussion

Although the circulation anomalies identified in this study suggest a potential linkage between North Atlantic SSTAs and large-scale atmospheric circulation variability over Eurasia, the present analysis is primarily statistical and diagnostic in nature. The wave-like circulation structures and upper-level wind anomalies associated with the NASSTI indicate that North Atlantic SST variability may modulate the Eurasian large-scale circulation background, thereby influencing atmospheric conditions favorable for TPV activity over the TP. However, the detailed dynamical processes responsible for this linkage remain unclear and require further investigation. More comprehensive dynamical analyses, such as Rossby wave source diagnostics, wave activity flux analysis, and numerical sensitivity experiments, would be helpful for clarifying the physical mechanisms and potential propagation pathways involved.

Author Contributions: L.X. and P.Q. contributed to the conceptualization, investigation, visualization, and writing of the manuscript. Z.Z., T.X., and X.L. contributed to the discussion of the results and the revision of the manuscript. All authors have read and agreed to the published version of the manuscript.

Funding: This study was supported by the National Natural Science Foundation of China (Grant No. 42505060).

Institutional Review Board Statement: Not applicable.

Informed Consent Statement: Not applicable.

Data Availability Statement: The TPV dataset used in this study was obtained from the National Tibetan Plateau Data Center (http://www.sciencedb.cn/dataSet/handle/556, accessed on 14 October 2024). Sea surface temperature, wind fields, pressure vertical velocity, horizontal wind divergence, and relative vorticity were derived from the ERA5 reanalysis produced by the European Centre for Medium-Range Weather Forecasts (ECMWF; https://www.ecmwf.int/en/forecasts/dataset/ecmwf-reanalysis-v5, accessed on 17 June 2024).

Acknowledgments: We acknowledge the National Tibetan Plateau Data Center and the European Centre for Medium-Range Weather Forecasts for providing the datasets used in this study.

Conflicts of Interest: The authors declare no conflicts of interest.

References

1. Li, Y.; Li, M.; Su, Y.; Li, Q.; Pang, S. Terrestrial net ecosystem productivity on the Tibetan Plateau: Characteristics, climate drivers and future changes. *Atmosphere* **2026**, *17*, 317. [CrossRef]
2. Zhou, T.; Zhang, W. Anthropogenic warming of the Tibetan Plateau and constrained future projection. *Environ. Res. Lett.* **2021**, *16*, 044039. [CrossRef]
3. You, Q.; Cai, Z.; Pepin, N.; Chen, D.; Ahrens, B.; Jiang, Z.; Wu, F.; Kang, S.; Zhang, R.; Wu, T.; et al. Warming amplification over the Arctic Pole and Third Pole: Trends, mechanisms and consequences. *Earth-Sci. Rev.* **2021**, *217*, 103625. [CrossRef]
4. Han, Y.Z.; Liao, J.; Zhao, Y.F.; Zhao, B.Y.; Zhao, S.; Ma, Y.M. Multi-sphere observation network and climate warming and humidification research on the Qinghai–Xizang Plateau: Advances and future directions. *Plateau Meteorol.* **2026**, *45*, 305–323. (In Chinese) [CrossRef]
5. Hong, J.; Kim, J. Scale-dependency of surface fluxes in an atmospheric mesoscale model: Effect of spatial heterogeneity in atmospheric conditions. *Nonlinear Process. Geophys.* **2008**, *15*, 965–975. [CrossRef]

6. Xiao, Z.; Duan, A. Impacts of Tibetan Plateau snow cover on the interannual variability of the East Asian summer monsoon. *J. Clim.* **2016**, *29*, 8495–8514. [CrossRef]
7. Zhao, P.; Zhou, X.; Chen, J.; Liu, G.; Nan, S. Global climate effects of the summer Tibetan Plateau. *Sci. Bull.* **2019**, *64*, 1–3. [CrossRef]
8. He, L.; Zhou, T.; Guo, Z.; Zuo, M.; Ren, Z.; Chen, X.; Wu, B.; Zou, L.; Zhang, L.; Man, W.; et al. Northward extension of the East Asian summer monsoon since the Miocene set by the uplift of the Tibetan Plateau. *Geophys. Res. Lett.* **2024**, *51*, e2023GL107262. [CrossRef]
9. Li, J.; Chen, W.; Zhou, T.; Liu, Y.; Huang, G.; Liu, X.; Hou, Z.; Ding, R.; Hu, P.; Chen, S.; et al. Progress in atmospheric circulation and climate system dynamics research in China over the past century. *Acta Meteorol. Sin.* **2025**, *83*, 582–636. [CrossRef]
10. Liao, J.; Yuan, F.; Zhao, P.; Han, Y.Z. Comparative evaluation of CRA reanalysis by using intensive radiosonde observations over the Qinghai–Xizang Plateau in summer. *Plateau Meteorol.* **2026**, *45*, 324–338. (In Chinese) [CrossRef]
11. Li, Z.; Gong, D. Spatiotemporal heterogeneity of intensifying extreme precipitation in China during the 21st century and its asymmetric climate response. *Atmosphere* **2026**, *17*, 330. [CrossRef]
12. Wu, G.; Tang, Y.; He, B.; Liu, Y.; Mao, J.; Ma, T. Potential vorticity perspective of the genesis of a TPV in June 2016. *Clim. Dyn.* **2022**, *58*, 3351–3367. [CrossRef]
13. Bai, A.; Bai, J.; Wang, Z.; Tu, C. Formation and precipitation processes of the southwest vortex impacted by the Plateau vortex. *Atmosphere* **2025**, *16*, 115. [CrossRef]
14. Lin, Z.Q.; Guo, W.D.; Jia, L.; Yao, X.; Zhou, Z. Climatology of Tibetan Plateau vortices derived from multiple reanalysis datasets. *Clim. Dyn.* **2020**, *55*, 2237–2252. [CrossRef]
15. Li, S.Y.; Lü, S.N.; Wen, J. Characteristics of Qinghai–Xizang Plateau vortex activities and identification of sensitive areas: A study on its correlation with the land surface. *Plateau Meteorol.* **2024**, *43*, 529–548. (In Chinese) [CrossRef]
16. Lin, Z.Q. Analysis of Tibetan vortex activities using 1979–2013 ERA-Interim reanalysis. *J. Meteorol. Res.* **2015**, *29*, 720–734. [CrossRef]
17. Lin, Z.Q.; Guo, W.D.; Ge, J.; Wu, R.-Q.; Du, J. Increased Tibetan Plateau vortex activities under 2 °C warming compared to 1.5 °C warming: NCAR CESM low-warming experiments. *Adv. Clim. Change Res.* **2021**, *12*, 322–332. [CrossRef]
18. Lin, Z.Q.; Guo, W.D.; Ge, J.; Yao, X.; Su, D. Interdecadal change of Tibetan Plateau vortices during the past four decades and its possible mechanism. *Clim. Dyn.* **2024**, *62*, 2971–2989. [CrossRef]
19. Yang, Y.C.; Li, Y.Q.; Chen, Y.R. The characteristic analysis of an eastwards Plateau vortex by its strengthening process. *Plateau Meteorol.* **2018**, *37*, 702–720. (In Chinese) [CrossRef]
20. You, Q.; Min, J.; Lin, H.; Pepin, N.; Sillanpää, M.; Kang, S. Observed climatology and trend in relative humidity over the central and eastern Tibetan Plateau. *J. Geophys. Res. Atmos.* **2015**, *120*, 3610–3621. [CrossRef]
21. Cong, N.; Shen, M.; Yang, W.; Yang, Z.; Zhang, G.; Piao, S. Varying responses of vegetation activity to climate changes on the Tibetan Plateau grassland. *Int. J. Biometeorol.* **2017**, *61*, 1433–1444. [CrossRef] [PubMed]
22. Curio, J.; Schiemann, R.; Hodges, K.I.; Turner, A.G. Climatology of Tibetan Plateau vortices in reanalysis data and a high-resolution global climate model. *J. Clim.* **2019**, *32*, 1933–1950. [CrossRef]
23. Yu, S.H.; Gao, W.L. Characteristics of surface land heating in the Qinghai–Tibetan Plateau vortex source regions for departing and non-departing Plateau vortices. *Plateau Meteorol.* **2019**, *38*, 299–313. (In Chinese) [CrossRef]
24. Liu, Y.; Lu, M.; Yang, H.; Duan, A.; He, B.; Yang, S.; Wu, G. Land–atmosphere–ocean coupling associated with the Tibetan Plateau and its climate impacts. *Natl. Sci. Rev.* **2020**, *7*, 534–552. [CrossRef]
25. Shen, H.; Gong, Z.; Liu, B.; Guo, Y.; Feng, X.; Wen, T.; Wang, X.; Feng, G. Remote effects of IOD and ENSO on motivating the atmospheric pattern favorable for snowfall over the Tibetan Plateau in early winter. *Front. Clim.* **2021**, *3*, 694384. [CrossRef]
26. Zhao, D.J.; Yao, X.P. Case study on shape evolution of Plateau shear line: Structural characteristics. *Plateau Meteorol.* **2018**, *37*, 420–431. (In Chinese) [CrossRef]
27. Sun, J.; Yao, X.; Deng, G.; Liu, Y. Characteristics and synoptic patterns of regional extreme rainfall over the central and eastern Tibetan Plateau in boreal summer. *Atmosphere* **2021**, *12*, 379. [CrossRef]
28. Zhou, S.; Sun, F.; Wang, M.; Zhou, S.; Qing, Y. Effects of atmospheric heat source on the Tibetan Plateau vortex in different stages: A case study in June 2016. *Atmosphere* **2022**, *13*, 689. [CrossRef]
29. Almahri, A.B.; Hasanean, H.M.; Labban, A.H. Spatiotemporal variability of tropical cyclone activity over the Arabian Sea (1982–2021): Tracks, energy metrics, and duration. *Atmosphere* **2026**, *17*, 389. [CrossRef]
30. Lin, L.; Zhuang, W.; Yang, Z.; Wang, H. Strengthened ENSO impact on January–April rainfall over southern India and Sri Lanka in recent decades. *Atmosphere* **2026**, *17*, 292. [CrossRef]
31. Yao, J.; Cen, L.; Zheng, M.; Sun, M.; Yin, J. Contrasting impacts of North Pacific and North Atlantic SST anomalies on summer persistent extreme heat events in eastern China. *Atmosphere* **2025**, *16*, 901. [CrossRef]
32. Cabrera, M.; Pezzi, L.; Santini, M.; Mendes, C. Quantifying the influence of sea surface temperature anomalies on the atmosphere and precipitation in the southwestern Atlantic Ocean and southeastern South America. *Atmosphere* **2025**, *16*, 887. [CrossRef]

33. Czaja, A.; Frankignoul, C. Influence of the North Atlantic SST on the atmospheric circulation. *Geophys. Res. Lett.* **1999**, *26*, 2969–2972. [CrossRef]
34. Ting, M.; Kushnir, Y.; Seager, R.; Li, C. Forced and internal twentieth-century SST trends in the North Atlantic. *J. Clim.* **2009**, *22*, 1469–1481. [CrossRef]
35. Deser, C.; Alexander, M.A.; Xie, S.P.; Phillips, A.S. Sea surface temperature variability: Patterns and mechanisms. *Annu. Rev. Mar. Sci.* **2010**, *2*, 115–143. [CrossRef] [PubMed]
36. Sheng, C.; He, B.; Wu, G.; Liu, Y.; Zhang, S.; Zhang, P. Interannual impact of the North Atlantic tripole SST mode on the surface potential vorticity over the Tibetan Plateau during boreal summer. *J. Geophys. Res. Atmos.* **2022**, *127*, e2021JD036369. [CrossRef]
37. Ma, T.; Wu, G.; Liu, Y.; Mao, J. Abnormal warm sea-surface temperature in the Indian Ocean, active potential vorticity over the Tibetan Plateau, and severe flooding along the Yangtze River in summer 2020. *Q. J. R. Meteorol. Soc.* **2022**, *148*, 1001–1019. [CrossRef]
38. Lin, Z.Q.; Guo, W.D.; Yao, X.P.; Zhou, Z.B. *Tibetan Plateau Vortex Dataset Derived from Multiple Reanalysis Data*; Science Data Bank: Beijing, China, 2018; V1. [CrossRef]